Predicting Frictional Properties of Graphene Kirigami Using Molecular Dynamics and Neural Networks

Designs for a negative friction coefficient.

Mikkel Metzsch Jensen

Thesis submitted for the degree of
Master in Computational Science: Materials Science
60 credits

Department of Physics
Faculty of mathematics and natural sciences

UNIVERSITY OF OSLO

Spring 2023

Predicting Frictional Properties of Graphene Kirigami Using Molecular Dynamics and Neural Networks

Designs for a negative friction coefficient.

Mikkel Metzsch Jensen

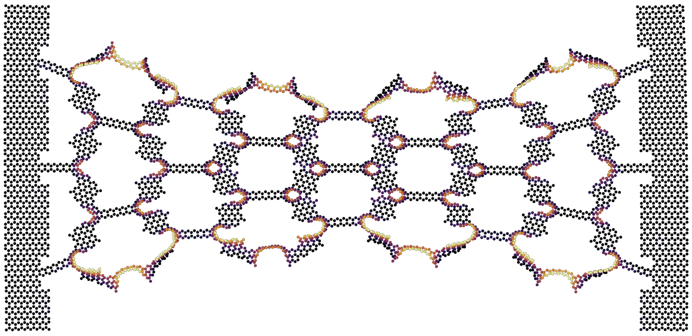

© 2023 Mikkel Metzsch Jensen

Predicting Frictional Properties of Graphene Kirigami Using Molecular Dynamics and Neural Networks

http://www.duo.uio.no/

Printed: Reprosentralen, University of Oslo

Abstract

Abstract.

Acknowledgments

Acknowledgments.

List of Symbols

F_N	Normal force (normal load)

Acronyms

CM Center of Mass. 10, 11

LJ Lennard-Jones. 15, 28

MD Molecular Dynamics. 5, 6, 9, 17, 20, 25, 26, 27

ML Machine Learning. 6, 27

std Standard Deviation. 12, 13, 16, 18

Contents

I Background Theory 1

II Simulations 3

1 Pilot study 5
  1.1 Friction simulation parameters 5
  1.2 Force traces 6
    1.2.1 Force oscillations 6
    1.2.2 Decompositions 10
    1.2.3 Center of mass path 10
  1.3 Defining metrics for friction 12
    1.3.1 Kinetic friction 12
    1.3.2 Static friction 13
  1.4 Out-of-plane buckling 14
  1.5 Investigating default parameters 16
    1.5.1 Computational cost 18
  1.6 Load and stretch dependencies 20
    1.6.1 Pressure reference for normal load 20
    1.6.2 Stretch dependencies 20
    1.6.3 Load dependency 23

2 Summary 25
  2.1 Summary and conclusions 25
    2.1.1 Design MD simulations 25
    2.1.2 Design Kirigami framework 26
    2.1.3 Control friction using Kirigami 26
    2.1.4 Capture trends with ML 26
    2.1.5 Accelerated search 27
    2.1.6 Negative friction coefficient 27
  2.2 Outlook / Perspective 28

Appendices 29

A Appendix A 31

A Appendix B 33

B Appendix C 35

Part I

Background Theory

Part II

Simulations

Chapter 1

Pilot study

Having defined our system, we carry out an initial study of the frictional properties. First, we evaluate the numerical results for a non-cut sheet in order to define suitable metrics for a numerical evaluation of friction and justify some of the default parameter choices. This provides a basis for the following study where we consider the Tetrahedron and Honeycomb Kirigami patterns as well. We conduct a more systematic investigation of the friction dependencies to temperature, sliding speed, spring constant and timestep. Finally, we consider the mean friction of all three configurations when stretched. This includes an analysis of the dependence to contact area and the friction-load curves.

1.1 Friction simulation parameters

The MD simulations we will carry out to measure friction are governed by a small set of parameters. For the purpose of creating a machine learning we need to standardize these parameters. This we keep most of them constant with only a small subset of parameters being varied: sheet configuration, strain and load. Instead of starting with the parameter selection process, we first state the final choice in Table 1.1. Due to the great number of parameters, we do not make an exhaustive search of all parameters before deciding on the final settings. Instead, we take a basis in parameters used in similar friction simulations [1–5] and adjust accordingly to the aim of getting stable measurements and reducing computation time where possible. Parameters such as initial relaxation time, pauses and strain speed are chosen mainly from the results of initial stability tests. The sheet and pull block sizes are chosen with a consideration of the balance between Kirigami design options and computational resources. The scan direction is chosen to be parallel to the connection line between the pull blocks. This is mainly chosen in order to avoid unessecary complexity in the motion since it can be hypothesized that the center of the sheet can drag behind for other scan directions. The remaining parameters: Temperature T, sliding speed v_{slide}, spring constant K, normal load F_N, timestep dt and sliding distance have been chosen because the friction output remains relatively stable with moderate perturbations around these default values. We will explain this in more detail later in the chapter. Note that the default values in Table 1.1 will be used when nothing else is stated explicitly.

Table 1.1: Parameters involved for the numerical MD simulation for measuring friction. The default values correspond to the final choice used for the dataset. The shaded cells denote the parameters varied in the ML dataset.

Parameter	**Default value**	**Description**
T	$300\,\mathrm{K}$	Temperature of the system.
v_{slide}	$20\,\mathrm{m/s}$	Sliding speed for the sheet translation.
K	∞	Spring constant for the coupling between the virtuel atom and the sheet pull blocks.
Scan direction	$(x, y) = (0, 1)$ (zigzag direction)	The direction for which we translate the sheet.
Sheet configuration	Contiguous	Binary mapping describing which atoms are removed (0) and which is still present (1) in the graphene sheet.
Strain amount	[0, rupture]	The ratio of change in length to the original length.
F_N	[0.1, 10] nN	Applied normal force to the pull blocks.
dt	$1\,\mathrm{fs}$	MD integration timestep.
Initial relaxation time	$15\,\mathrm{ps}$	Initial relaxation time before straining.
Pauses	$5\,\mathrm{ps}$	Relaxation pauses after strain, and during the normal load phase (before translating the sheet).
Strain Speed	$0.01\,\mathrm{ps}^{-1}$	The rate of straining for the sheet.
Slide distance	$400\,\text{Å}$	How far the sheet is translated.
Sheet size	$130.029 \times 163.219\,\text{Å}$	Spatial 2D size of the sheet.
Pull block size	$2 \times 130.029 \times 15.183\,\text{Å}$	Spatial 2D size of the pull blocks.

1.2 Force traces

We begin by assessing the friction force traces, i.e. force vs. time curves, for a single friction simulation using the default parameters shown in Table 1.1 for a non-cut sheet with no stretch applied and a normal load of $1\,\mathrm{nN}$.

1.2.1 Force oscillations

We evaluate the friction force as the force acting on the sheet from the substrate. We consider initially the force component $F_{\parallel}$ parallel to the drag direction as plotted in Fig. 1.1. We use a sample rate of $10\,\mathrm{ps}^{-1} = 100\,\mathrm{timesteps}^{-1}$ for which each sample is the mean value of the preceding 100 timesteps. We observe immediately that the data carries oscillations on different time scales which match our general expectations for sliding involving periodic surfaces. By applying a Savgol filter to the data with a polynomial order of 5 and a window length of 150 timesteps (corresponding to a sliding distance of $3\,\text{Å}$ or a time window of $15\,\mathrm{ps}$) we can qualitatively point out at least two different frequencies of oscillation. During the first 10 Å of sliding, seen in Fig. 1.1a, we see roughly three waves on the Savgol filter corresponding to a relatively high frequency, while for the duration of 100 Å of sliding, seen in Fig. 1.1b, the same Savgol filter reveals a lower frequency on top, creating the visual pattern of a wavepacket. The data does not indicate clear signs of stick-slip behavior as otherwise found in other studies, e.g. by Zhu and Li [4] for graphene on gold, who saw a more typical saw tooth shape in the force trace. Besides the difference in the substrate material, using gold instead of silicon, they used a lower sliding speed of $10\,\mathrm{m/s}$ and a soft spring of $K = 10\,\mathrm{N/m}$. By adopting these parameters we get a slightly different force trace behavior as shown in Fig. 1.1c and Fig. 1.1d. This change breaks the symmetry in the force oscillations but still does not produce any significant discontinuities in the trace. By keeping the spring constant $K = 10\,\mathrm{N/m}$ and lowering the sliding speed further down to $1\,\mathrm{m/s}$ we are able to demonstrate a proper stick-slip behavior as shown in Fig. 1.1e and Fig. 1.1f. Considering all three simulations we might classify the results from the default settings, $K = \inf, v = 20\,\mathrm{m/s}$, as smooth sliding, $K = 10\,\mathrm{N/m}, v = 10\,\mathrm{m/s}$, as a transition phase with possible occasional slipping, and $K = 10\,\mathrm{N/m}, v = 1\,\mathrm{m/s}$ as certain stick-slip behaviour. This confirms the qualitative observation the stick-slip behavior is suppressed with stiff springs [6] springs and high sliding velocity [3]. Having a low sliding speed comes with a high computational cost which is the reason that we choose a relatively high sliding speed of 20 m/s. The choice of an infinite spring constant is related to the stability of the measurements and is discussed later in this chapter make sure it is, maybe make a reference.

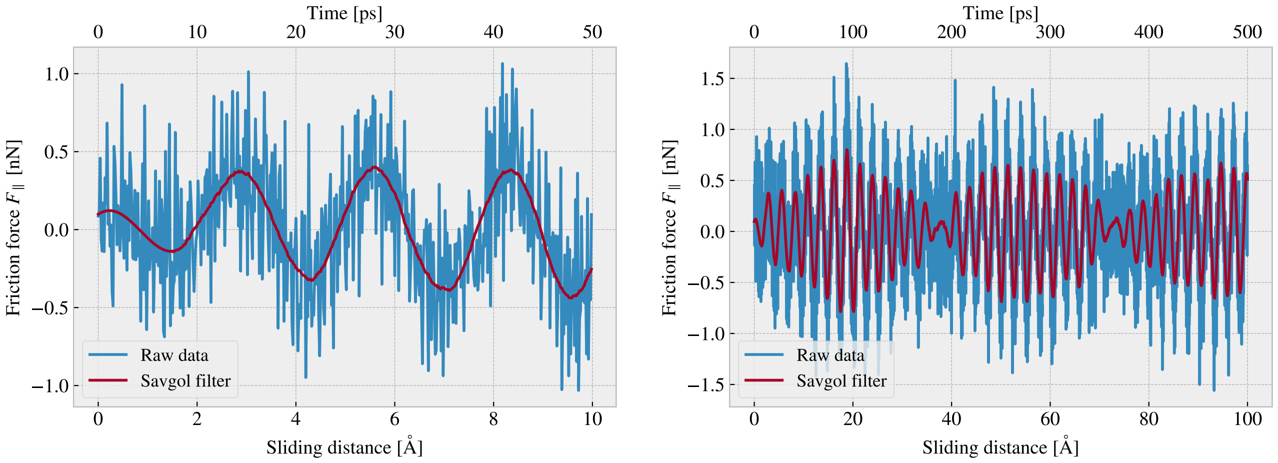

(a) $K = \text{inf}$, $v = 20\,\frac{\text{m}}{\text{s}}$ (10 Å sliding).

(b) $K = \text{inf}$, $v = 20\,\frac{\text{m}}{\text{s}}$ (100 Å sliding).

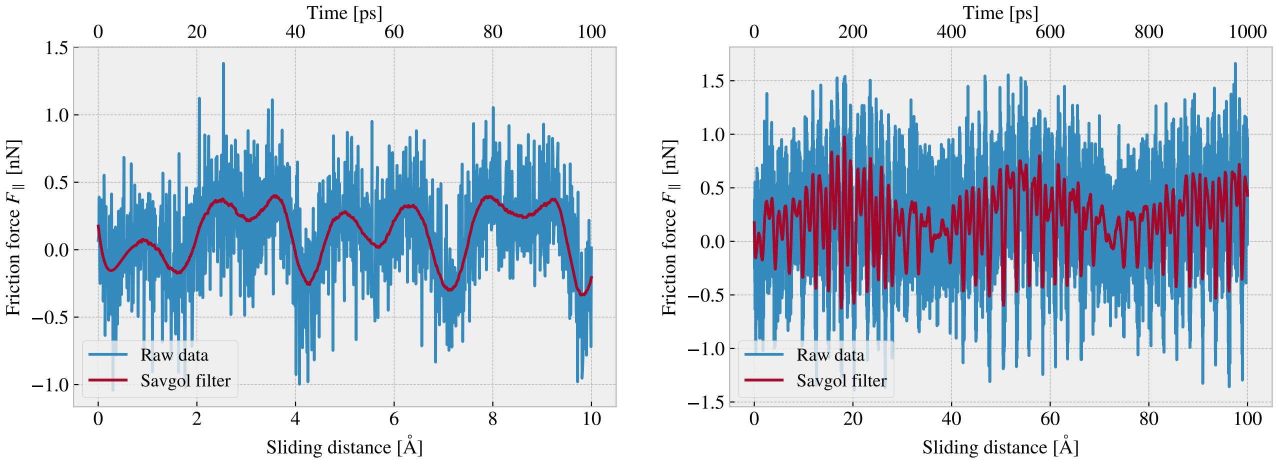

(c) $K = 10\,\frac{\text{N}}{\text{m}}$, $v = 10\,\frac{\text{m}}{\text{s}}$ (10 Å sliding).

(d) $K = 10\,\frac{\text{N}}{\text{m}}$, $v = 10\,\frac{\text{m}}{\text{s}}$ (100 Å sliding).

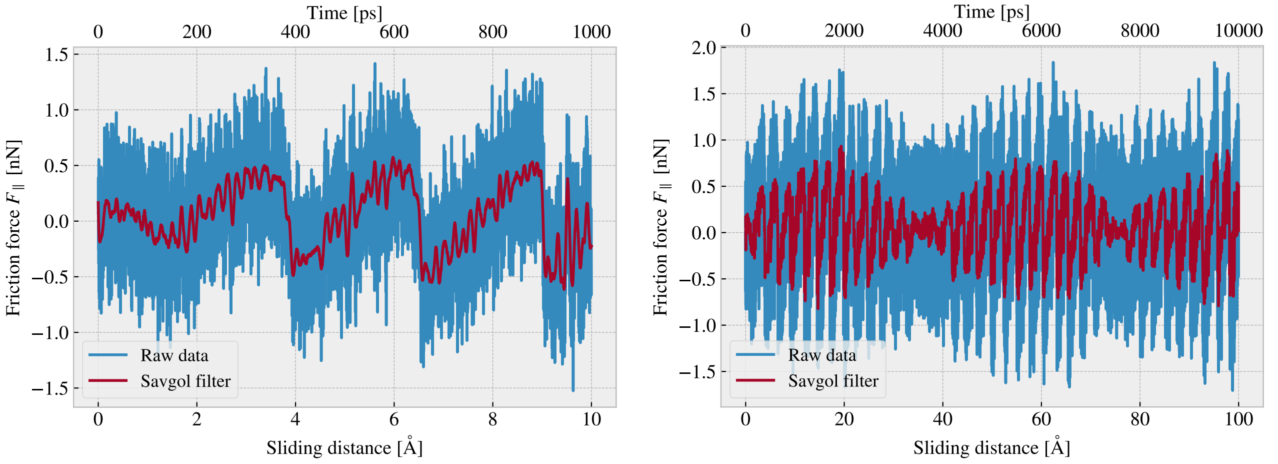

(e) $K = 10\,\frac{\text{N}}{\text{m}}$, $v = 1\,\frac{\text{m}}{\text{s}}$ (10 Å sliding).

(f) $K = 10\,\frac{\text{N}}{\text{m}}$, $v = 1\,\frac{\text{m}}{\text{s}}$ (100 Å sliding).

Figure 1.1: Force traces of the friction force $F_\parallel$ with respect to the drag direction acting from the substrate on the full sheet. The force traces are plotted against the sliding distance (lower x-axis) and the corresponding sliding time (upper x-axis). The sliding distance is measured by the displacement of the virtual atom tethering the sheet. The red line represents a Savgol filter with polynomial order 5 and a window length of 150 timesteps (corresponding to a sliding distance of 3 Å or a time window of 15 ps). Each row, (a,b), (c,d), (e,f), represents a different choice of the spring constant K and sliding speed v, while the columns show the same result for two different time scales. The default settings are represented in figure (a) and (b).

By performing a Fourier Transform on the data, using the default parameters, we can quantify the leading frequencies observed in figure Fig. 1.1a and Fig. 1.1b. The Fourier transform is shown in Fig. 1.2a, and by plotting the two most dominant frequencies $f_1 = 0.0074\,\mathrm{ps}^{-1}$ and $f_2 = 0.0079\,\mathrm{ps}^{-1}$ as a sine sum, $\sin(2\pi f_1) + \sin(2\pi f_2)$, we find a qualitatively convincing fit to the observed wavepacket shape as seen in Fig. 1.2b. We can convert the frequencies according to that of a wavepacket. By using the trigonometric identity

$$\begin{aligned}\sin(a+b) &= \sin(a)\cos(b) + \cos(a)\sin(b),\\ \sin(a-b) &= \sin(a)\cos(b) - \cos(a)\sin(b),\end{aligned}$$

and decomposing the frequencies as $f_1 = a - b$, $f_2 = a + b$, we can rewrite the sine sum as the sinusoidal product

$$\begin{aligned}\sin(2\pi f_1) + \sin(2\pi f_2) &= \sin\big(2\pi(a-b)\big) + \sin\big(2\pi(a+b)\big)\\ &= \sin(2\pi a)\cos(2\pi b) + \cancel{\cos(2\pi a)\sin(2\pi b)} + \sin(2\pi a)\cos(2\pi b) - \cancel{\cos(2\pi a)\sin(2\pi b)}\\ &= 2\sin(2\pi a)\cos(2\pi b),\end{aligned}$$

with

$$\begin{aligned} a = \frac{f_1+f_2}{2} &= 0.0763 \pm 0.0005\,\mathrm{ps}^{-1}, & b = \frac{f_2-f_1}{2} &= 0.0028 \pm 0.0005\,\mathrm{ps}^{-1},\\ &= 0.381 \pm 0.003\,\text{Å}^{-1}, & &= 0.014 \pm 0.003\,\text{Å}^{-1}.\end{aligned}$$

In the latter transition, we have denoted the frequency with respect to the sliding distance by considering the default sliding speed of $20\,\mathrm{m/s} = 0.2\,\text{Å}/\mathrm{ps}$. This makes us recognize the high oscillation frequency as a and the low frequency as b. The faster one has a period of $T_a = 2.62 \pm 0.02$ Å [1] which corresponds well with the magnitude of the lattice spacing and especially that of graphene at 2.46 Å as expected theoretically. The longer period $T_b = 71 \pm 15$ Å is not obviously explained. We notice a similarly long period oscillation for all three cases Fig. 1.1b, Fig. 1.1d and Fig. 1.1f, and thus we have no reason to believe that this is dependent on the stick-slip behavior. The initial build-up in friction force is reminiscent of friction strengthening, which is often reported [1, 7], but the periodicity goes against this idea. Instead, we might attribute it to some phonon resonance which could be a physical phenomenon or simply a feature of our MD modeling.

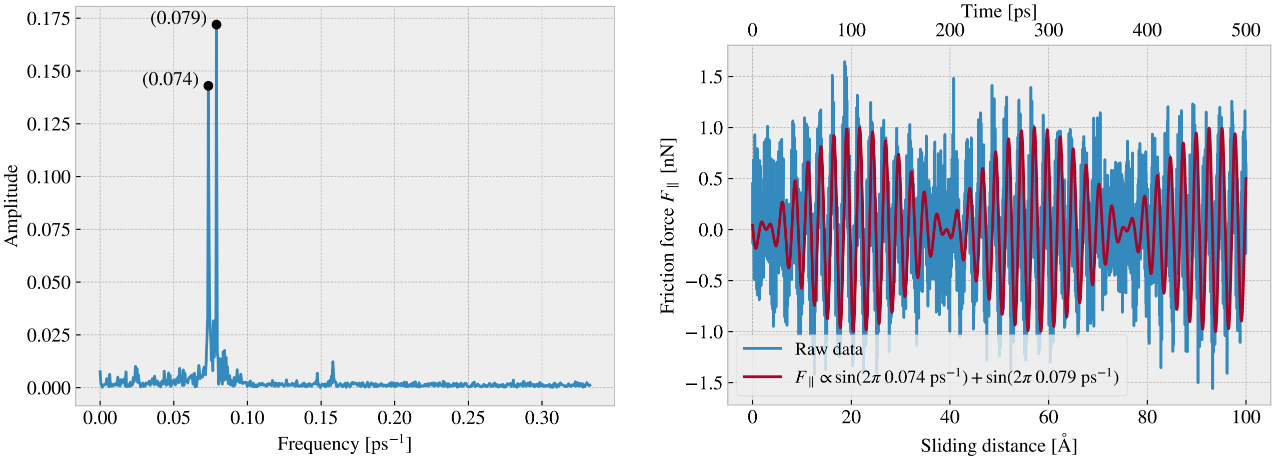

(a) FT result shown for a reduced frequency range.

(b) Two most dominant frequencies applied to the data from Fig. 1.1b

Figure 1.2: Fourier transform analysis of the full friction force data (all 400 Å sliding distance) shown in Fig. 1.1. (a) shows the two most dominant frequency peaks. Note that no significant peaks was found in a higher frequency than included here. (b) shows a comparison between the raw data and the wavefunction corresponding to the two peaks in figure (a).

---

[1] The uncertainty Δy is calculated as $\Delta y = \left|\frac{\partial y}{\partial x}\Delta x\right|$ for uncertainty Δx and $y(x)$

1.2.2 Decompositions

In the previous analysis, we looked only at the friction force for the full sheet, including the rigid pull blocks, and with respect to the drag direction. We found this way of measuring the friction force to be the most intuitive and reliable, but we will present the underlying arguments for this choice in the following.

Since we are only applying cuts to the inner sheet, and not the pull blocks, it might appear more natural to only consider the friction inner sheet. If the desired frictional properties can be achieved by altering the inner sheet one can argue that any opposing effects from the pull blocks can be mitigated by simply scaling the relative size between the inner sheet and the pull blocks. However, when looking at the force traces decomposed with respect to the inner sheet and pull block regions respectively in Fig. 1.3a, we observe that the friction force arising from those parts is seemingly antisymmetric. That is, the distribution of the frictional pull from the substrate on the sheet is oscillating between the inner sheet and the pull blocks. Keeping in mind that normal force is only applied to the pull blocks we might take this as an intrinsic feature of the system that does not necessarily disappear with a scaling of the spatial ratio between the inner sheet and pull blocks. Any interesting friction properties might depend on this internal distribution of forces. Hence, we hedge our bets and use the full sheet friction force as a holistic approach to avoid excluding relevant information in the measurement data.

Similarly, we might question the decision of only considering the frictional force projected onto the sliding direction as we are then neglecting the "side shift" induced during sliding. In Fig. 1.3b we show the decomposition in terms of the force components parallel $F_{\|}$ and perpendicular $F_{\perp}$ to the sliding direction respectively. We notice that the most dominant trend appears for the parallel component. If we want to include the perpendicular component as well we would have to evaluate friction as the length of the force vector instead. However, this would remove the sign of the force direction and shift the mean friction force up as we see both negative and positive contributions in the parallel force trace. One option to accommodate this issue is by using the vector length for the magnitude but keeping the sign from the parallel component. However, we omit such compromises as this might make the measurement interpretation unessercary complex, and we use only the parallel component going forward.

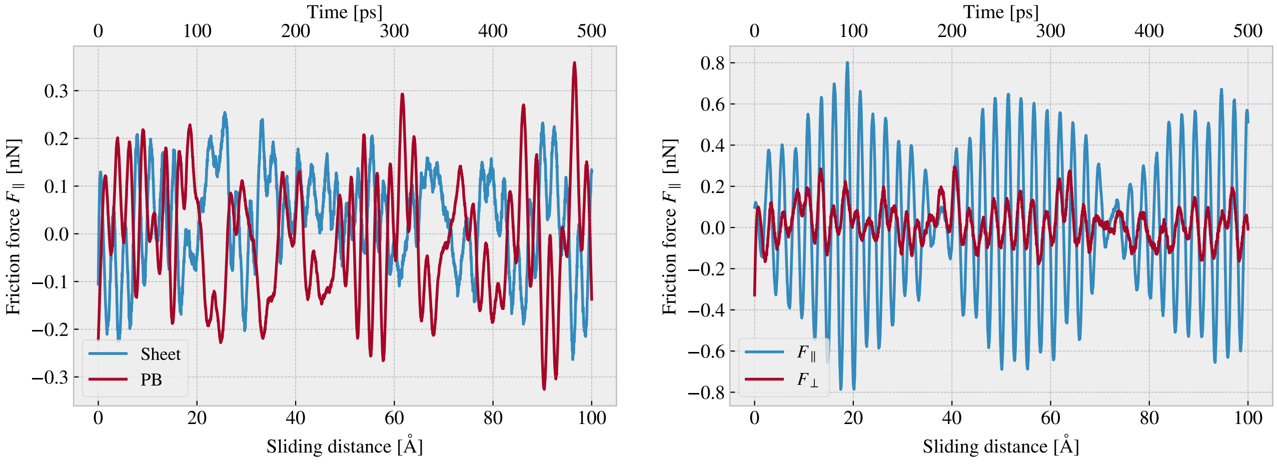

(a) **(b)**

Figure 1.3: Friction force decomposition on the default parameter force trace shown in Fig. 1.1 showing only the applied Savgol filters. (a) Decomposition into group inner sheet (sheet) and pull blocks (PB). (b) Decomposition into parallel ($F_{\|}$) and perpendicular ($F_{\perp}$) to drag sliding direction.

1.2.3 Center of mass path

From the previous observations of the force traces in Fig. 1.1 we found both smooth sliding and stick-slip behavior depending on the sliding speed and spring constant. Considering the force decomposition in Fig. 1.3b we know that a frictional force in the perpendicular direction to sliding is also present. By looking at the x, y-position for the sheet Center of Mass (CM) we find a qualitatively different behavior when reconsidering the spring constants and sliding speeds investigated in Fig. 1.1. These results are shown in Fig. 1.4. The default case in Fig. 1.4a shows a rather straight path forward with only a small side motion in comparison to the cases in Fig. 1.4b and Fig. 1.4c. However, the CM accelerates and deaccelerates with a high frequency, much too high to be associated with the lattice spacing on the order of 2.46 Å. One possible explanation is that the sheet and substrate constitute an incommensurable contact for which traveling kink excitations make the atoms move in such a way that the sheet CM is incremented in small "burst". When looking at the $K = 10\,\frac{\text{N}}{\text{m}}$, $v = 10\,\frac{\text{m}}{\text{s}}$ case in Fig. 1.4b we see a completely different CM path where the rapid movements aligns visually better with the force oscillations shown earlier in Fig. 1.1d. The CM accelerates forward and then deaccelerates in combination with a side motion that leads to the CM path making a loop as it slows down. Finally we have the $K = 10\,\frac{\text{N}}{\text{m}}$, $v = 10\,\frac{\text{m}}{\text{s}}$ in Fig. 1.4b which is confirmed to have stick-slip behavior in Fig. 1.1f. Here the CM path shows a more chaotic movement between acceleration, but with the rapid parts aligning which also visually well with the timing of the slips seen in Fig. 1.1f. The chaotic motion is not connected to the stick-slip motion, but we might associate it with the thermal contributions being dominant in this regime.

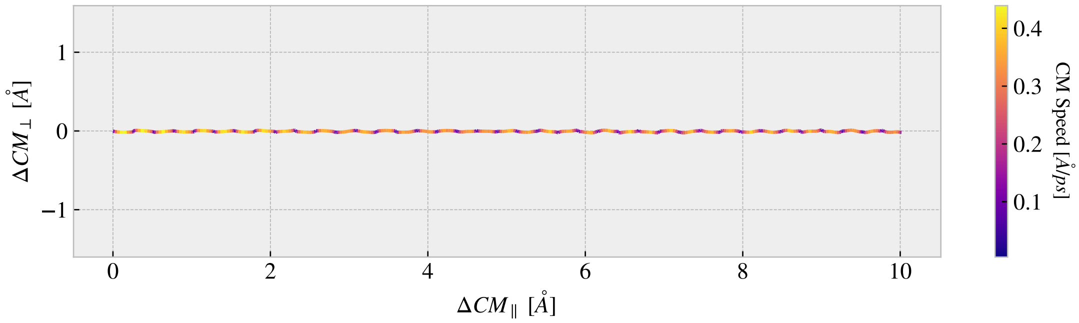

(a) $K = \text{inf}$, $v = 20\,\frac{\text{m}}{\text{s}}$.

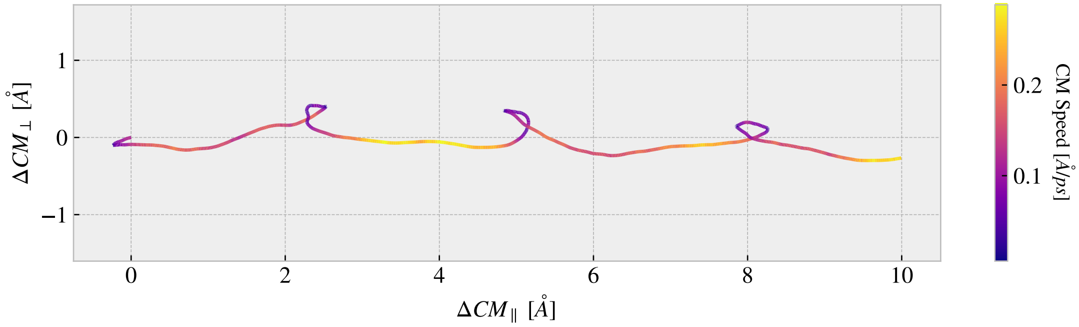

(b) $K = 10\,\frac{\text{N}}{\text{m}}$, $v = 10\,\frac{\text{m}}{\text{s}}$.

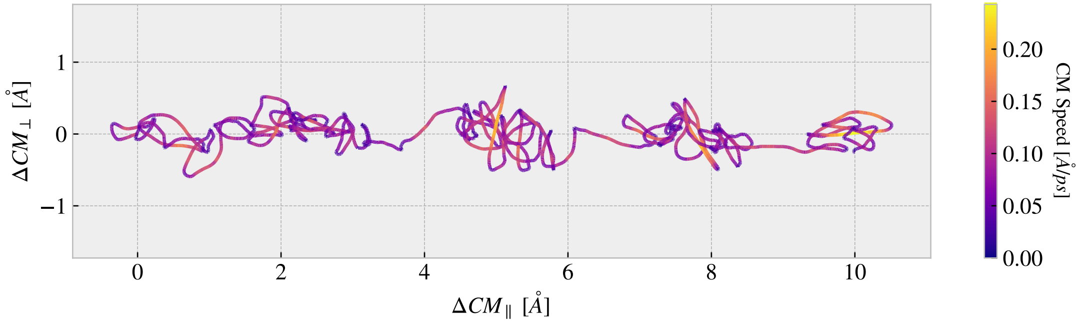

(c) $K = 10\,\frac{\text{N}}{\text{m}}$, $v = 1\,\frac{\text{m}}{\text{s}}$.

Figure 1.4: Center of Mass (CM) position relative to the start of the sliding phase in terms of the direction parallel to the sliding direction $\Delta COM_\parallel$ and the axis perpendicular to the sliding direction $\Delta COM_\perp$. The colorbar denotes the absolute speed of the CM motion. Figure a-c shows different parameters used for the spring constant K and sliding speed v similar to that used in Fig. 1.1. (a) Default: $K = \text{inf}$, $v = 20\,\frac{\text{m}}{\text{s}}$. (b) $K = 10\,\frac{\text{N}}{\text{m}}$, $v = 10\,\frac{\text{m}}{\text{s}}$. (c) $K = 10\,\frac{\text{N}}{\text{m}}$, $v = 1\,\frac{\text{m}}{\text{s}}$

1.3 Defining metrics for friction

In order to evaluate the frictional properties of the sheet we aim to reduce the force trace results, addressed in section Sec. 1.2, into single metrics describing the kinetic and static friction respectively.

1.3.1 Kinetic friction

We measure kinetic friction as the mean of the friction force trace. More precisely, we take the mean value of the last half of the dataset in order to ensure that we are sampling from a stable system. For a full sliding simulation of 400 Å our mean value will be founded on the last 200 Å (1000 ps) of sliding. In Fig. 1.5a we have shown the force trace for the first 10 Å of sliding together with a 50% running mean window. The choice of such a short sliding distance is merely to illustrate the sampling procedure, and we see that the final mean estimate (marked with a dot) takes a negative value due to the specific cut-off of the few oscillations captured here. Nonetheless, one approach to quantify the uncertainty of the final mean estimate is to consider the variation of the running mean preceding the final mean value. The more the running mean fluctuates the more uncertainty associated with the final estimate. Only the running mean "close" to the ending should be considered, since the first part will rely on data from the beginning of the simulation. From the Fourier analyze in section Sec. 1.2.1 we found the longest significant oscillation period to be ~ 71 Å. Hence, we find it reasonable to use the standard deviation (std) for the last ~ 71 Å of the running mean window to evaluate the fluctuations. When including the full sliding length this corresponds to the last $\sim 35\%$ of the running mean window. We consider the std as an estimate of the absolute error and calculate the relative error by a division of the final mean value. In Fig. 1.5b we showcase a running relative error based on the std, with a window of length 35% the mean window, in a continuation of the illustrative case of a 10 Å sliding from Fig. 1.5a. In this case, we get an extremely high relative error of $\sim 257\%$, but this is consistent with the fact that the short sampling period leads to an unphysical negative value which should be associated with high uncertainty.

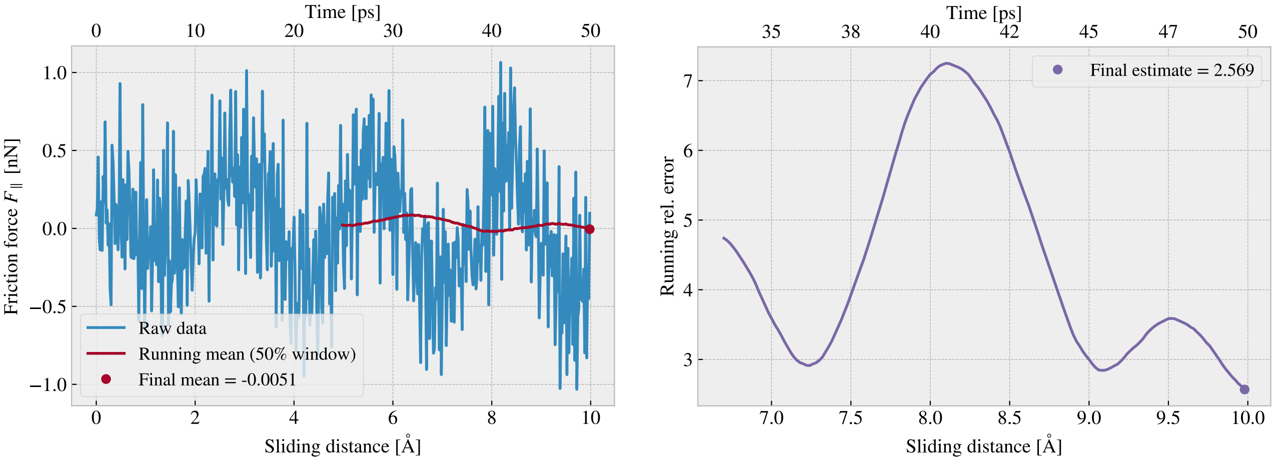

(a) Running mean with window length 5 Å (50% the data length).

(b) Running std with window length 1.75 Å (35% the mean window length.)

Figure 1.5: Running mean (a) and running relative error (std) (b) on the friction force data from a reduced sliding distance of 10 Å. The running mean window is 50% the data length while the running std window is 35% the running mean window length. The values are plotted at the end of their respective windows such that windowprecedess the actual point on the graph.

When including the full dataset of 400 Å of sliding, such that the std window actually matches with the longest period of oscillations expected, we get a final relative error of $\sim 12\%$ as shown in fig Fig. 1.6. This is arguable just at the limit of an acceptable error, but as we shall see later on in Sec. 1.6 this high relative error is mainly associated with the cases of low friction. When investigating different configurations under variation of load and strain we see a considerably lower relative error as the mean friction evaluates to higher values. One interpretation of this finding is simply that the oscillations in the running mean are to some degree independent of the magnitude of the friction. In that case, the relative error will spike for the low friction cases, and the absolute error might be the more reliable measure, i.e. using simply the std without dividing by the final mean value.

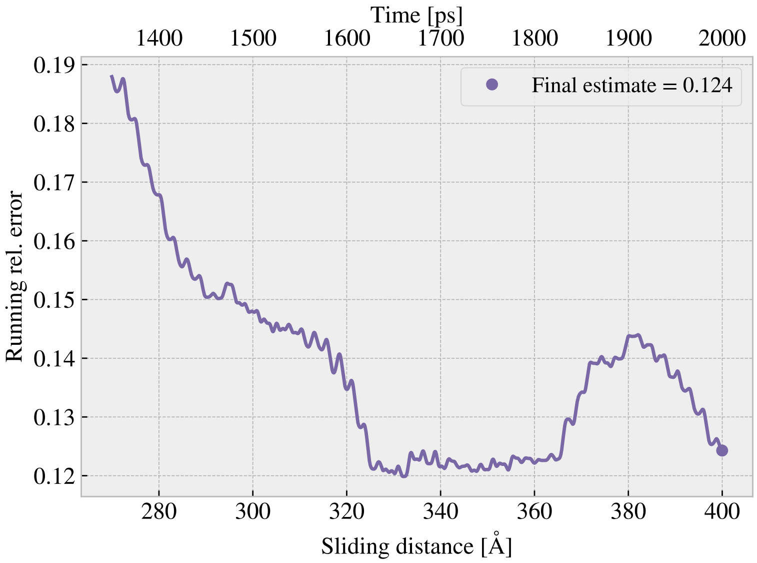

Figure 1.6: Running standard deviation (std) for a full 400 Å sliding simulation. The running std window is 70 Å (35% the running mean window of 50% the data length).

1.3.2 Static friction

The maximum value is one of the common choices for addressing static friction, even though the definition of static friction is a bit vague. When considering the force traces in Fig. 1.1 we observe that the force oscillations increase in magnitude toward a global peak at ~ 20 Å. Thus, one could be inclined to identify this peak as the maximum value associated with the static friction force. However, as we have already clarified, this steady increase in friction is part of a slower oscillation that repeats by a period of ~ 71 Å. By plotting the top three max values recorded during a full 400 Å simulation, for 30 logarithmically spaced load values in the range $[0.1, 100]$ nN, we observe that the global max rarely falls within this first oscillation period as shown in Fig. 1.7. Only 2 out of 30 global maxima and 4 out of 90 top three maxima can be associated with the start of the sliding by this definition. Thus, this result suggests that our default system does not yield a static friction response in the sense of an initial increase in friction due to a depinning of the sheet from the static state. Some parameter changes that might increase the likelihood of seeing a significant static friction response are either extending the relaxation period since static friction is theorized to increase logarithmically with time [8], or increasing the sliding force more slowly through a soft spring tethering. As an attempt to test the latter part of this hypothesis we run a series of simulations with varying spring constant, $K \in [5, 200]$ nN including also $K = \infty$, but keeping the relaxation time and sliding speed at the default values. The result is shown in Fig. 1.8 and do not show any support for the hypothesis that a softening of the spring constant will eventually lead to the friction maximum occurring in the first period of sliding. We note that this might be suppressed by having a too short relaxation period or a too high sliding speed (related to the initial force increase), but due to the ambiguousness in the assessment of the static friction we will mainly concern ourselves with the kinetic friction in the remaning of this thesis.

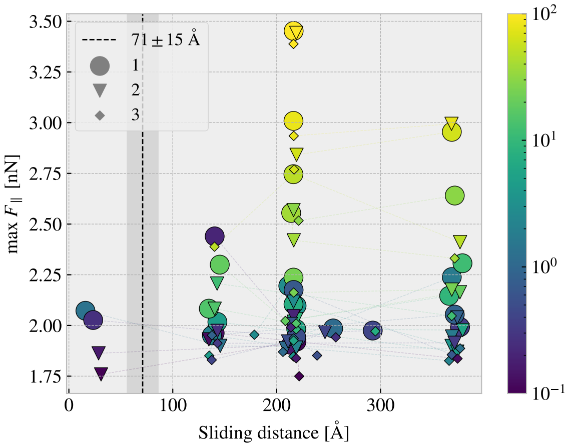

Figure 1.7: Distribution of top three max friction force peaks for 30 uniformly sampled normal forces $F_N \in [0.1, 10]$ nN. The dotted line and the grey area mark the slowest significant oscillation period found in the data and thus marking a dividing line for whether a peak falls within the "beginning" of the sliding simulation.

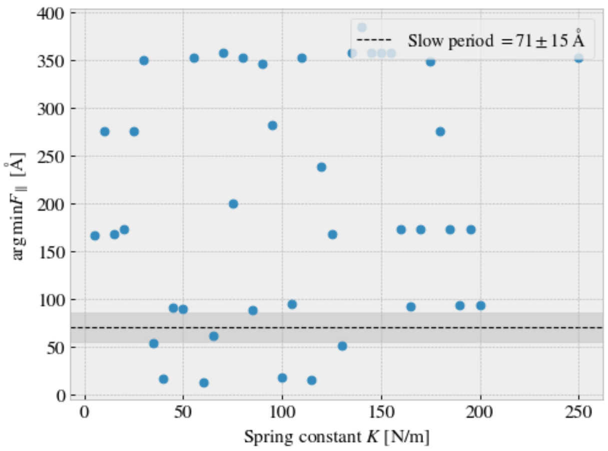

Figure 1.8: Sliding displacement for the max friction peak to appear as a function of spring constant. Fixmove is tmp mapped to K = 200 here without any discontinuous lines.

1.4 Out-of-plane buckling

The out-of-plane buckling is one of the motivations for investigating the application of Kirigami cuts in the context of friction properties. Therefore, we perform a stretch simulation, at low temperature ($T = 5\,\mathrm{K}$) without any substrate, in order to verify that we can reproduce an out-of-plane buckling with the Tetrahedron and Honeycomb patterns intended for our study (see **??**). For this investigation we consider the Tetrahedron $(7, 5, 1)$ and the Honeycomb $(2, 2, 1, 5)$ pattern in comparison to the non-cut sheet. We quantify the out-of-plane buckling by assessing the distribution of atoms along the z-direction (perpendicular to the plane) during stretching. We calculate the minimum and maximum z-value as well as the atom count quartiles 1%, 10%, 25%, 50% (median), 75%, 90% and 99% as shown in Fig. 1.9. The results show significant buckling for the Tetrahedron and Honeycomb patterns in comparison to the non-cut sheet which only exhibits minor buckling of ~ 2 Å which is on the same order as the lattice spacing. Moreover, we notice that the Tetrahedron pattern buckles more in consideration to the min. and max. peaks while the remaining quantiles seem to be more closely spaced than for the Honeycomb. By addressing the simulation results visually, using the *Open Visualization Tool OVITO*, we find that this can be attributed to fringes on the edge "flapping around" and thus increasing the min. and max. values.

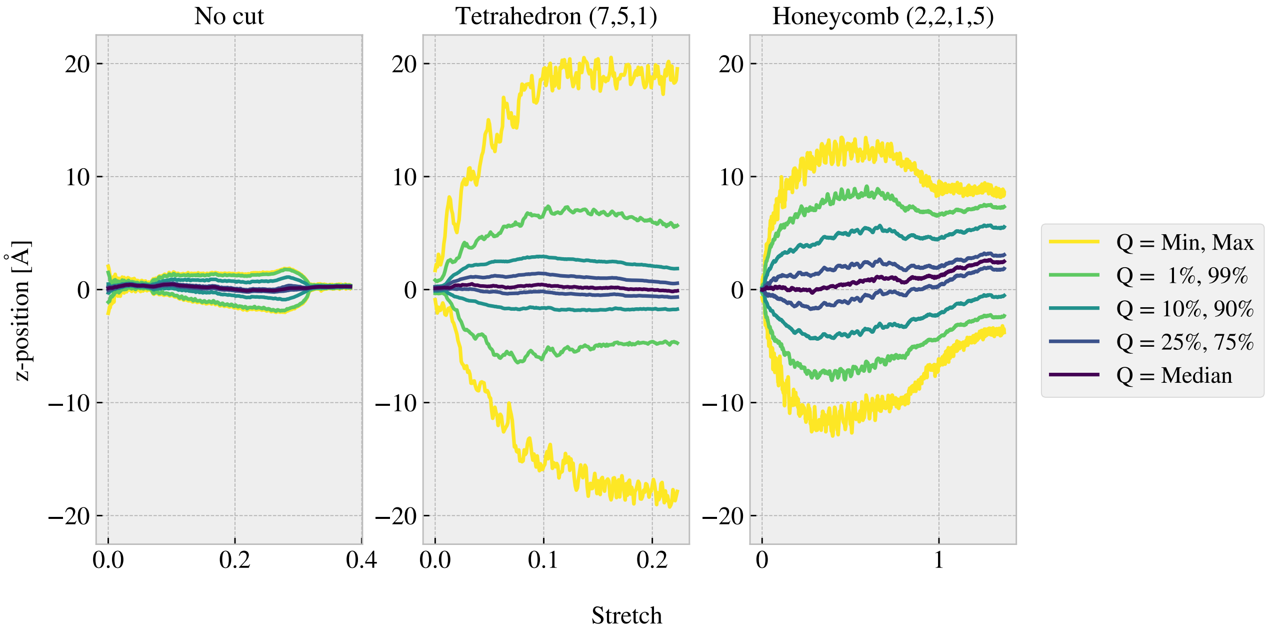

Figure 1.9: Out-of-plane buckling during stretching of the No cut, Tetrahedron $(7, 5, 1)$ and Honeycomb $(2, 2, 1, 5)$ sheet resepctively in vacuum at low temperature $T = 5\,\mathrm{K}$. The buckling is measured by the distribution of the atom z-position (perpendicular to the sheet plane), for which the colors indicates selected quantiles. The yield strain were, reading from left to right, 0.38, 0.22 and 1.37.

Given the confirmation of out-of-plane buckling in a vacuum, as seen in Fig. 1.9, we reintroduce the substrate in order to investigate whether this effect carries over to a changing contact area. For this simulation we raise the temperature to the default value of $T = 300\,\mathrm{K}$. We keep the normal force off and let the sheet stick purely by the adhesion forces between the sheet and substrate. We quantify the contact area through the relative amount of atoms in the sheet within chemical range of the substrate. The cut-off for this interaction is set to 4 Å, inspired by [1], corresponding to $\sim 120\%$ the LJ equilibrium distance. Usually, the contact area is calculated as the number of contacting atoms multiplied by an associated area for each atom. However, since we are not interested in the absolute value of the area, but rather the relative change, we omit the multiplication factor. That is, we consider the relative number of atoms within the contact range, which is proportional to the contact area, as our metric of choice. The relative contact for the three configurations (No cut, Tetrahedron $(7, 5, 1)$ and Honeycomb $(2, 2, 1, 5)$) during strecthing are shown in figure Fig. 1.10. The figure reveals a significant drop in contact as the sheets are stretched, which agrees qualitatively with the buckling observed in Fig. 1.9 without the substrate. The Honeycomb pattern turns out to be both the most stretchable, with a rupture strain of 1.27, and the one with the biggest decrease in relative contact with a minimum of approximately 43%. Notice, that the relative contact is never actual 1.0 but instead reaches a maximum of 96% with no stretching. This is attributed to the temperature fluctuations and the choice of cut-off. Thus we might

Selected frames from the simulation result are shown in **??** which reveals a bit more information on how the buckling occurs. The Tetrahedron pattern deforms rather quickly and smoothly into small tetrahedron spikes, as the name suggests. In the Honeycomb pattern, on the other hand, the deformations initiate from one side first. As the sheet stretches more rows of the pattern are activated, producing the honeycomb-looking shape when seen from above. Both patterns exhibit a small increase in relative contact when they are approaching their yield strain, which agrees with the results from Fig. 1.9 where the buckling reduces slightly towards the rupture strain.

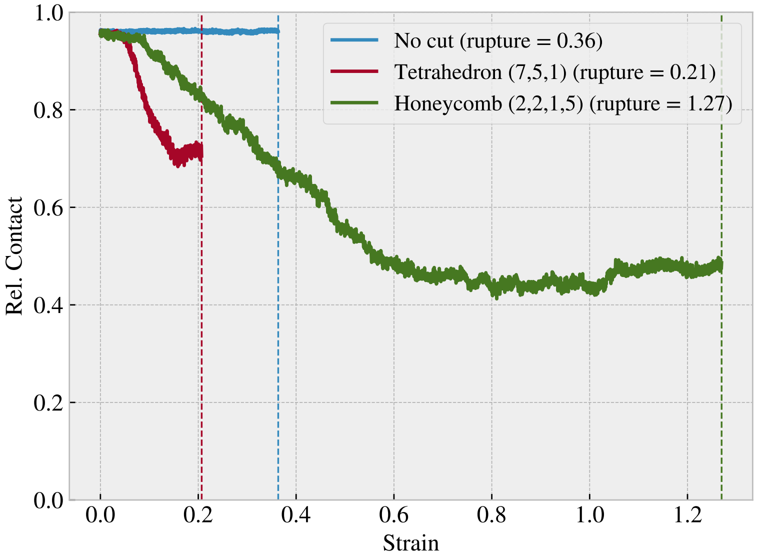

Figure 1.10: Relative contact, given as the relative number of atoms in the sheet being within chemical interaction range, vs. strain of the sheet. The cut-off for the interaction range is 4 Å corresponding to $\sim 120\%$ the LJ equilibrium distance. No normal force is applied and temperature is kept at $T = 300\,\mathrm{K}$.

Compare figure Fig. 1.10 to that of figure ?? where multiple simulations constitute the stretch-contact curve.

1.5 Investigating default parameters

We carry out a more extensive investigation of the friction dependence on temperature T, sliding speed v_{slide}, spring constant K, and timestep dt. This is done partly to understand how the dependencies relate to the theoretical, numerical and experimental results, and partly to understand how these parameters affect the stability of our system. We use the default parameters presented in Table 1.1 and investigate the results as we change parameters, one at a time. We keep the load at 1 nN. We consider the mean friction force, sampled from the last half of the simulation as described in Sec. 1.3, representing the kinetic friction. The results are shown in Fig. 1.11, where the shaded area (connected linearly) denotes the absolute error defined by the std as described in Sec. 1.3.

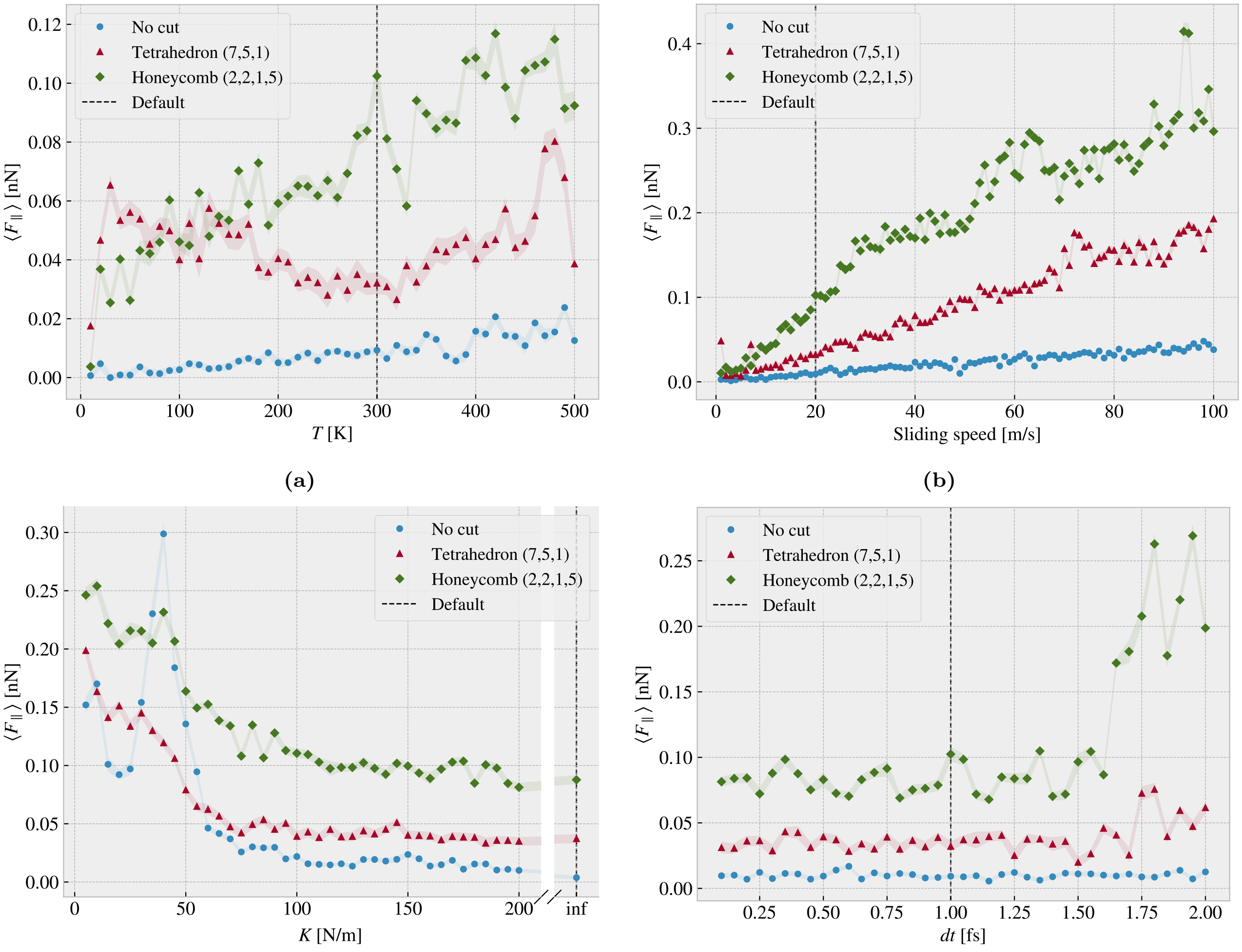

(a) **(b)**

(c) **(d)**

Figure 1.11: Main parameters investigation. Kinetic friction force

From the temperature investigation in Fig. 1.11a we find an increasing kinetic friction with temperature for both the non-cut sheet and the Honeycomb pattern. The Tetrahedron pattern shows both decreasing and increasing trends. The general trend shows a convex curve in the range (30–480 K) with a minimum around our default choice of 300 K, but with rapid fluctuations at the start (10–30 K) and end region (480–500 K). Similar fluctuations are also seen from the Honeycomb pattern, although it shows an underlying increasing trend throughout. When comparing the non-cut sheet and the Honeycomb pattern we observe that the slope for the increasing trend is high for the Honeycomb. From a theoretical and experimental point of view, we would expect a decrease in friction with temperature (see **??**). However, an increasing trend is also observed in other MD simulation, for instance by Zhang et al. [5] sliding at 10 m/s, which is attributed to the high sliding speed associated with the ballistic motion. The default choice is initially based on the common choice of using the temperature $T = 300\,\mathrm{K}$. The non-cut and Tetrahedon friction seems to be rather stables around that point, but we do see some significant fluctuations for the Honeycomb pattern in this range. However, we do not regard this as a critical feature.

From the sliding speed investigation in Fig. 1.11b we generally find increasing friction with velocity. Due to the relatively high velocities used and the effects from the thermostat, we expect a viscous friction $F_k \propto v_{\text{sliding}}$ which matches rather well with these results. However, the Tetrahedron and Honeycomb sheets seem to fall slightly into a sublinear relationship as it approaches higher velocities. Furthermore, these sheets display indications of local fluctuations that could potentially be attributed to resonance effects, as discussed in relation to the phonon dynamics. Our choice of sliding speed at 20 m/s mainly reflects a consideration of computational cost, but the fact that no immediate resonance fluctuations appear in the proximity of this value supports the choice.

From the investigation of the spring constant parameter in Fig. 1.11c we observe a significant decrease in friction as the springs stiffen. This can be attributed to the transition from a stick-slip influenced regime to a smooth sliding regime as we saw for the force traces in Fig. 1.1. For soft springs the results are quite sensitive to the specific choice of spring constant which is especially seen for the non-cut sheet around $K = 40\,\mathrm{N/m}$. Thus, in order to avoid this domain we settled for the infinitely stiff spring. This is also considered a more favorable option due to its ability to provide greater standardization of the simulations.

Finally, we consider the numerical stability of the result as we vary the simulation timestep in Fig. 1.11d. The general trend shows a stable plateau below $\sim 1.5\,\mathrm{fs}$ for which higher values show signs of arising instabilities for the cut sheets (Tetrahedron and Honeycomb). This mainly confirms that our choice of timestep is within a reasonable range. However, we do see some fluctuations which are more significant for the cut sheets.

The observed fluctuations suggest that randomness plays a role in our simulations and also indicate that the cut sheets are relatively unstable. Further investigation through varying the random seed for the initial velocity and thermostat could shed more light on this matter. In the meantime, we may consider these fluctuations as a sign that the uncertainty in our results is higher than what was estimated using the running mean and running std evaluation For the Honeycomb sheet, these fluctuations are on the order $\pm 0.017\,\mathrm{nN}$

1.5.1 Computational cost

We run the simulations on a CPU cluster made available by the University of Oslo. This allows us to run multiple simulations at once and with each simulation running in parallel on multiple CPU cores as well. As we decide on the simulation parameters we must also consider the computational cost. When selecting simulation parameters, we also need to keep in mind the computational cost. Given that the chosen parameters will be applied to multiple simulations, any increase in computational time will be multiplied by the number of intended simulations, which is expected to be around 10,000. The computational cost is especially dependent on the timestep and the sliding speed as this will affect the number of computations. As an extension of the analysis in Sec. 1.5 we report on the computational times associated with temperature, sliding speed, spring constant and dt. By retrieving the computational time used for the parameter investigation in Fig. 1.11 we get the timing as shown in Fig. 1.12. Note that these timings are only based on a single simulation for each parameter as opposed to an average over multiple runs which is nessecary for more reliable data.

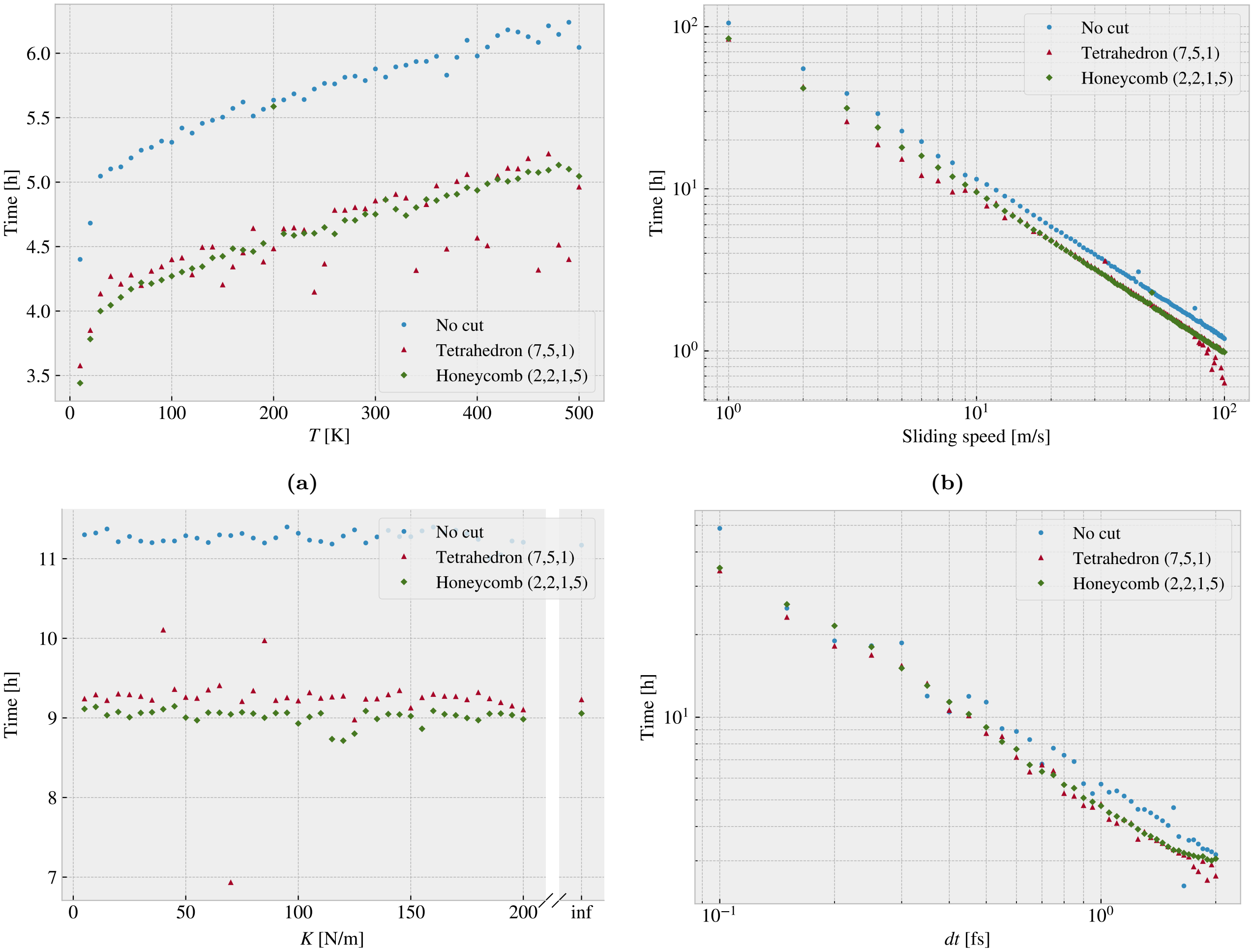

(a) **(b)**

(c) **(d)**

Figure 1.12: Computational cost related to temperature, sliding speed, spring constant and dt parameter in terms of CPU hours running on 16 cores on the cluster. Sliding speed follows $t \propto v^{-0.977 \pm 0.005}$ and dt follows $t \propto \mathrm{dt}^{-0.87 \pm 0.02}$

The computational time is governed by the number of timesteps in the simulation and the time used per timestep. For a fixed sliding distance, the number of timesteps in the simulation are inversely proportional to sliding speed and similar inversely proportional to timestep dt. From the timings in Fig. 1.12 we find the sliding speed to obey this expectation rather well by $t \propto v^{-0.977 \pm 0.005}$ while the timing did not increase as strongly with timestep, falling below the $1/dt$ relation with $t \propto \mathrm{dt}^{-0.87 \pm 0.02}$. Moreover, we find that increasing temperature also makes for an increased computation time. This can be attributed to an increase in the computation time associated with the force calculations. The rising temperature gives rise to more fluctuations in the system which might yield more atoms within the force calculation cutoffs for each computation. This kind of consideration can also be attributed to the reason for the deviating timing for dt. Finally, for the spring parameter, we did not see any noticable effect on timing.

In general, we have selected our simulation parameters: temperature, sliding speed, spring constant, and timestep, based on numerical stability and computational cost. For the timestep, we found that a value of 1 fs, commonly used in similar studies [3, 4], produced stable results while higher values were prone to instabilities and lower values were computationally expensive. The sliding speed was chosen primarily based on computational cost, with a default value of 20 m/s being a reasonable compromise between computational efficiency and the lower values more commonly used in other studies. Although a lower sliding speed could lead to more commonly observed stick-slip motion, it represents a factor of 20 increase in computational time. Since stick-slip motion is out of reach based on the chosen sliding speed, we found that using an infinitely stiff spring $K = \infty$ was the most reasonable option to ensure stable results. Finally, the temperature investigation did not provide much guidance for a specific choice, so we settled for the standard choice of room temperature $T = 300\,\mathrm{K}$.

1.6 Load and stretch dependencies

So far, we have carried out a general analysis of the system behaviour under different parameters which lays the foundation for the remaining study. We now shift our intention towards the friction dependence of load and stretch.

1.6.1 Pressure reference for normal load

We consider a load range of 0.1–10 nN which alligns with the general choice in other MD studies SOURCE. In order to relate to the magnitude of this load we provide a short calculation of the corresponding pressure. We will use the pressure underneath a stiletto heeled shoe as a high pressure reference from our macroscale world. The diameter of a stiletto heeled shoe can be less than 1 cm [9], and hence an 80 kg man[2] standing on one stiletto heel, with all the weight on the heel, will correspond to a pressure

$$P = \frac{F}{A} = \frac{mg}{r^2\pi} = \frac{80\,\mathrm{kg}\cdot 9.8\,\frac{\mathrm{m}}{\mathrm{s}^2}}{(\frac{10^{-2}\,\mathrm{m}}{2})^2\pi} = 9.98\,\mathrm{MPa}.$$

The fact that the pressure under a stiletto heel can get this high, actually greater than the pressure under an elephant food, is in an interesting realization in itself that is often used in introductory physics courses [10], but this also serves as a reasonible upperbound for human executed pressure. With a full sheet area of $\sim 21 \times 10^3\,\text{Å}^2$ our load range of 0.1–10 nN corresponds to a pressure of 0.47–47 MPa which relates nicely with our macroscale reference. This pressure might be incompatible with various industrial purposes, but with no specific application in mind this serves as a decent reference point. Notice that if we consider a human foot with area $113\,\mathrm{cm}^2$ [11] the pressure drops to a mere 70 kPa corresponding to only $\sim 0.01\,\mathrm{nN}$.

1.6.2 Stretch dependencies

We consider the effects of stretching the sheet using the non-cut, Tetrahedron $(7, 5, 1)$ and Honeycomb $(2, 2, 1, 5)$ sheet as used so far. For each configuration, we run a rupture test where the given sheet is stretched under zero load, but still under the influence of adhesion from the substrate. The rupture strain is then recorded, and multiple new simulations are initiated with strain values between zero and the rupture strain. For the sampling of the stretch values in the available range, we use a pseudo-uniform distribution, meaning that we divide the given interval into equal segments and pick a value from each segment by a uniform distribution. This is due to numerical limitations in LAMMPS[3], but we find that this gives evenly spaced values which also carry some randomness. For the load we use 0.1, 1 and 10 nN.

First, we aim to reproduce the contact investigation from Fig. 1.10. We quanitify the relative contact as described in Sec. 1.4, but converts this into a single metric for a given simulation by considering the average of the last 50% of data points, similar to what we have done for the mean friction, and we adopt the same method for quantifing the error. The results are shown in Fig. 1.10 where we observe a significant decrease in contact for the kirigami patterns which qualitatively agrees with the non-loaded continous stretch investigation from Fig. 1.10. This result implies that the change in contact can not be related to a momentum effect during stretching, as each simulation now keeps the stretching constant throughout the simulation. The absolute error for the mean rel. contact were generally quite low on the order of 0.01 for all configurations.

From an asperity theory point of view this reduction in contact is theorized to induce a similar reduction in friction, but when considering the kinetic friction shown in Fig. 1.13b we find that this is definitely not the case. As the contact decreases, for the Tetrahedron and Honeycomb pattern, the friction increases. Yet, these are not simply inversely proportional. The friction force suddenly dips down and up again, around 0.08–0.11 for the Tetrahedron and 0.73–1.05 for the Honeycomb pattern. This suggests that the contact area is not a dominating mechanism for friction in this system. The absolute error for the mean friction measure was fairly low on the order of 0.001–0.01 nN.

---

[2] Yes, a man can certainly wear stilleto heels.

[3] In LAMMPS, we sample the various strain values by storing restart files during the straining of the sheet. The restart values are stored at specific timesteps governed by a LAMMPS variable. Such variables allow for a vector of uniform randomly chosen values, but unfortunately, we are not able to sort the vector for ascending values. This will lead to the script waiting to store each restart file according to the timesteps in the unsorted vector. As soon as the next timestep value is less than the current timestep the program will stop producing restart files and thus skip most of them. However, by first defining a series of intervals we can draw a uniform number for each interval without getting into trouble.

We notice also that the two orders of magnitude increase in normal load did not make a significant difference in the results. In a study by Zhang et al. [7] they found that straining the sheet lead to a reduction in friction. Despite the fact that our result suggest an increase in friction with straining we notice that the observed effect is only present for the kirigami sheets, while the friction force on the non-cut sheet shows no appreciable dependency on the stretching.

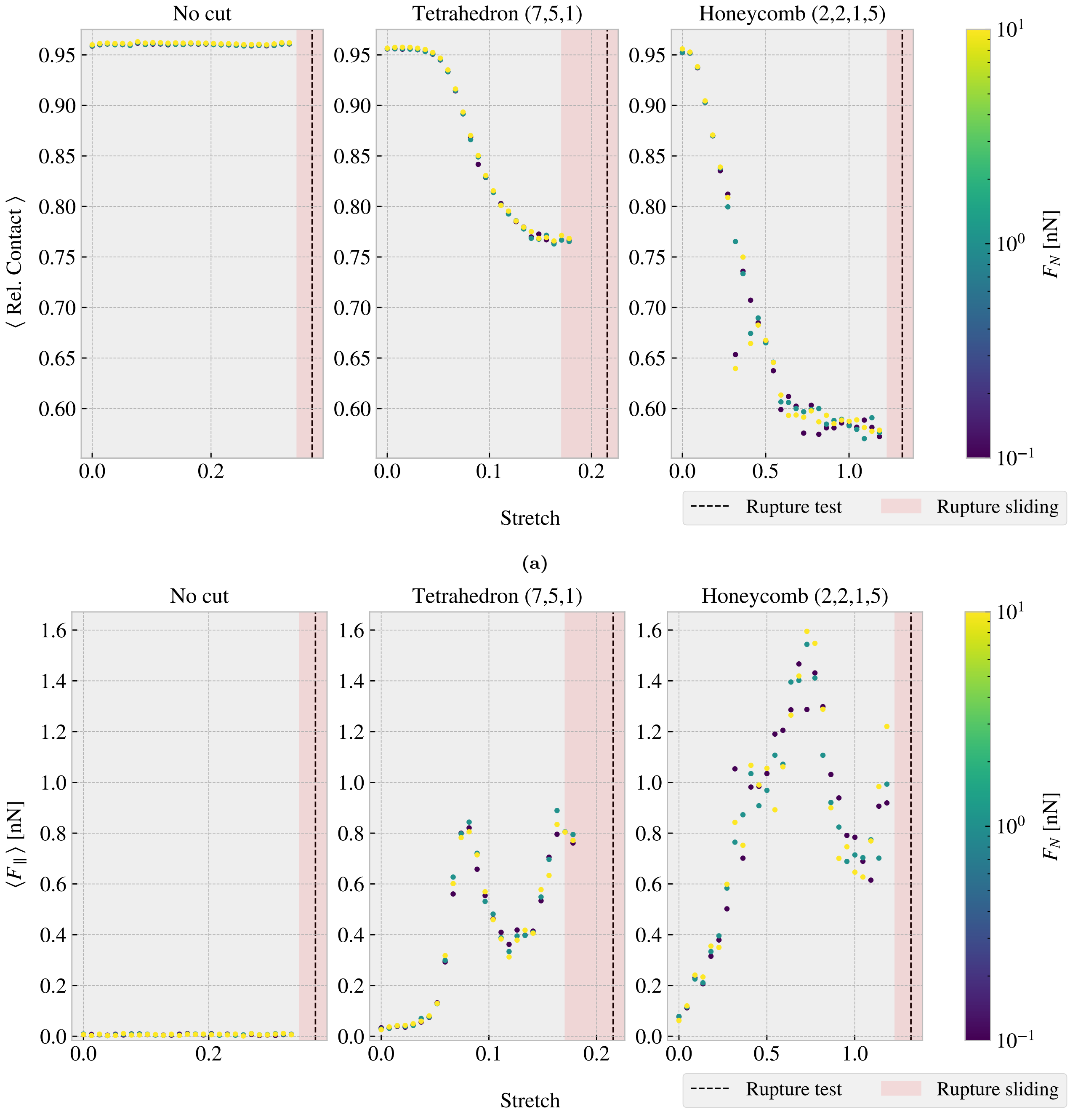

(a)

(b)

Figure 1.13: Average relative contact and average friction for multiple simulations, consisting of 30 stretch values sampled from a pseudo uniform distribution between 0 and the rupture point in combination with loads 0.1, 1 and 10 nN, for each of the configurations: non-cut, Tetrahedron $(7, 5, 1)$ and Honeycomb $(2, 2, 1, 5)$. The average is taken over the last half of the sliding phase. The red shade denotes the stretch range where ruptures accoured during sliding while the black-dotted line represent the rupture point in the no load rupture test. (a) The average relative contact defined as the relative number of atoms within a contact threshold of 4 Å to the substarte. The absolute error is on the order 0.01 (b) The average mean friction force parallel to the sliding direction. The absolute error is on the order 0.001–0.01 nN

By considering the increase in friction from no stretch towards the first peak we find that the Tetrahedron pattern exhibit a relative increase of ~ 27.7 while the Honeycomb pattern exhibit a relative increase of ~ 22.4. This is in itself a remarkable result, but considering that the friction drops almost as dramatically down again is even more unexpected. These results are thus promising for the prospect of demonstrating a negaive friction coefficients by altering the stretch through a coupling to the load.

Henrik: Her kan du godt skrive litt mer. Poengtere akkurat hvor mye friksjonen faller. Og spekulere litt i hvordan man kan bruke dette til ae designe noe med negativ friksjonskoeffisient.

1.6.3 Load dependency

From the investigation of the stretch dependency we saw that increasing the normal load from 0.1 to 10 nN did not make a considerable impact on the friction in comparison to the effect associated with stretch. One special feature of our system is that we only apply load to the pull blocks, and thus one might suspect this to be of importance. Therefore, we investigate the friction under varying load for a non-cut sheet comparing the case of loading the pull block against a more traditional uniform loading of the sheet as shown in Fig. 1.14. Both load distribution shows a seemingly non-dependent relationship considering the size of our estimated error. Nevertheless, we do not see any indications that the uniform loading changes the qualitative behaviour.

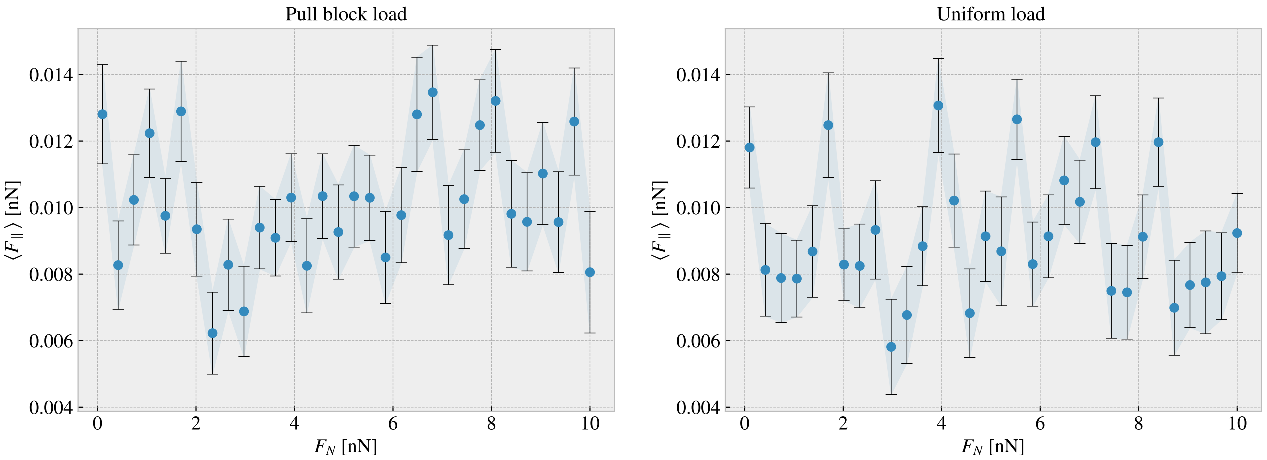

(a) **(b)**

Figure 1.14: Multiple simulations of non-cut sheet under different load. Mean friction is plotted against load for two different variations of loading distribution. (a) Normal loading is applied to the pull blocks. (b) Normal loading is applied uniformly to the sheet.

In order to investigate the friction dependency of normal load for the kirigami patterns as they are stretched, we select a subset of stretch stages from Fig. 1.13b and perform additionally simulations with a logarithmically increasing normal load in the extended range 0.1–100 nN, using 30 load points for each stretch. The results are shown in Fig. 1.15. Now, when spanning three orders of magnitude for load, we start to see a noticable increase in friction. This goes for all patterns, but it is only really visible for the non-cut sheet as the friction axis is a lot more zoomed in. Due to the fact that we have plotted the normal load on an logarithmic axis any seemingly linear trends on the figure is in fact sublinear. However, as the normal load approaches 100 nN we do start to se an increase that is more remniscent of a linear relationship, but this is difficult to judge given that the change in friction is small in comparison to the noise in the data. Note that we omitted the error bars for visual purposes but they are one the same order of magnitude as shown in Fig. 1.14.

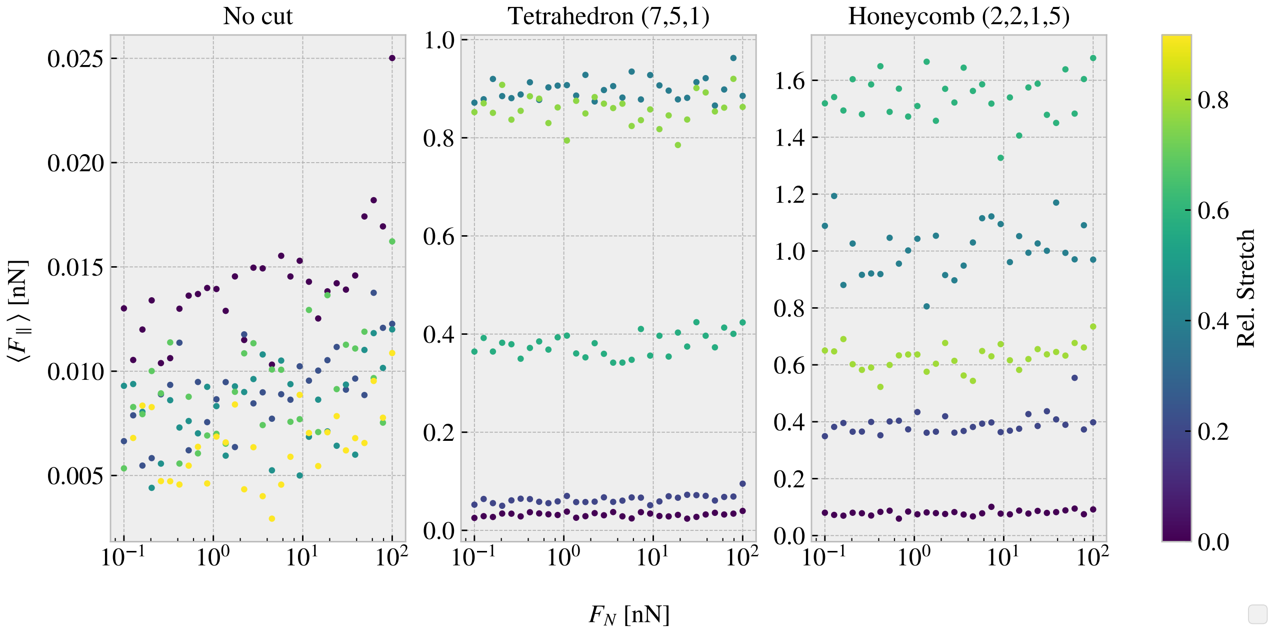

Figure 1.15: Mean friction force vs. load in the range 0.1–100 nN, for the non-cut, Tetrahedron $(7,5,1)$ and Honeycomb $(2,2,1,5)$ sheet resepctively, at different stretch stages relative to their rupture point.

From the friction measurements in Fig. 1.15 we see that the non-cut sheet generally produce a friction force in the order of 0.005–0.0025 nN throughout the 0.1–100 nN load range. Using a ratio based friction coeffcient definition **??**, $\mu_1 = F_{\text{fric}}/F_N$, this would lead to a coefficient roughly in the range

$$\mu_1,\ \textbf{??}: \quad \text{No cut} \sim [10^{-4}, 0.13], \quad \text{Tetrahedron} \sim [4\times 10^{-4}, 8.7], \quad \text{Honeycomb} \sim [9\times 10^{-4}, 15.2].$$

However, these values mainly reflect the poornes of this definition, as we find the values to diverge at low load and decrease towards high load due to the lacking linear relationship and an offset in the load curve corresponding to a finite friction at zero load. This offset is drastically enhanced for the kirigami patterns under applied stretch. Due to the small changes in friction compared to the noise in the data, it is not sensible to calculate the slope dF_{fric}/dF_N as a function of load. Nonetheless, if we force a linear fit for the whole range and use the second definition **??** as $\langle \mu_2 \rangle = \Delta F_{\text{fric}}/\Delta F_N$, we get average coefficients in the range

$$\mu_2,\ \textbf{??}: \quad \text{No cut} \sim [4,9]\times 10^{-5}, \quad \text{Tetrahedron} \sim 5\times[10^{-5}, 10^{-4}], \quad \text{Honeycomb} \sim [1,9]\times 10^{-4},$$

depending on the stretch values. These numbers should be interpreted cautiously, but we can interpret it as a rough estimate of the friction coefficient being on the order 10^{-4}–10^{-5}. This relates to the finding by [12] who reported a seemingly non-existing relationship between friction and normal load with change in friction that corresponds to a friction coefficients in the range 10^{-3}–10^{-4} when using the slope definition **??**. This supports the idea that the graphene sheet does in fact exhibit superlubric behavior in these conditions. Moreover, the fact that the increase with load is relatively unaffected by the stretching points to the fact that the stretch-induced effect mainly shifts the load curve towards higher friction but does not significantly alter its slope. Considering the big difference in the ratio for the demonstrated friction changes with stretch (for the kirigami patterns) and the friction coefficients, we can conclude that the stretch-induced mechanism is dominating the friction response. This works well with the idea of creating a nanomachine that couples load and stretch. By applying load on the nanomachine we would increase both the load and the strain on the sheet simultaneously. However, since the friction dependency to strain dominates in comparison to load effects such a system can be designed entirely by considering the strain dependency.

Chapter 2

Summary

The work presented in this thesis covers several topics (find a better opening line?). We have created an MD simulation which enabled us to study the frictional behavior of a graphene sheet sliding on a Si substrate. In addition, we have created a numerical framework for creating Kirigami design patterns and introducing these into the friction simulations. This was used to study the effects of the out-of-plane buckling induced by a selected pair of Kirigami designs in relation to a non-cut sheet under the influence of strain. Further, we have created a dataset of various Kirigami designs for the scope of investigating the possibilities with Kirigami design. We have investigated the possibility to use machine learning on this dataset and attempted an accelerated search. Finally we look into the prospects of achieving a negative friction coefficient for a system with coupled load and stretch. In this chapter we will summarize the findings and draw some final conclusions. We will also provide some topics for further research.

2.1 Summary and conclusions

2.1.1 Design MD simulations

We have designed an MD simulation for the examination of friction for a graphene sheet sliding on a silicon substrate. The key system features were the introduction of the pull blocks, defined as the end regions of the sheet with respect to the sliding direction, which was utilized for applying normal load and sliding the sheet. The pull blocks were made partly rigid and used to employ a thermostat as well. Similarly, we divided the substrate into three parts with the lowermost part being rigidly locked in place, the middle part reserved for a thermostat and the upper part remaining free from further modifications. By an analysis of the friction forces from a sliding simulation we settled on a standardization of the kinetic friction metric as the mean value of the last half of the sliding simulation. This was measured with respect to the sliding distance and for the full sheet (including the pull blocks). We defined the uncertainty of the measurements through the standard deviation of the running mean. We found that the assessment of static friction was ambiguous for our simulation and did not pursue this further. From the analysis of the force traces, friction force vs. time, we identify the friction behavior in our simulation domain as being in the smooth sliding regime. This is further supported by a demonstration of a transition to stick-slip behavior for softer springs and lower sliding speed which points toward our system being in the ballistic sliding regime. By conducting a more systematic investigation of the effects of temperature, sliding speed, spring constant and timestep, we settled on standardized choices based on numerical stability and computational cost. We found that friction increased with temperature which disagrees with experimental and theoretical considerations but matches other MD. This is attributed to simulation conditions corresponding to a ballistic regime. We choose a room temperature 300 K as a standard choice. We found friction to increase with velocity as expected with some signs of phonon resonance sliding speeds as well. We chose a rather high velocity of 20 m/s mainly for the consideration of computational cost. For the spring constant, we found decreasing friction with increasing stiffness of the springs which is associated with the transition from a stick-slip-influenced regime toward smooth sliding. The choice of an infintely stiff spring was made from a stability assessment. Finally, we confirmed that a timestep of 1 fs provides reasonable numerical stability. However, some fluctuations were observed, especially for the Honeycomb pattern, which might be interpreted as a sign of a higher uncertainty than expected on the order of ±0.017 nN.

2.1.2 Design Kirigami framework

We have desgined a numerical framework for creating Kirigami designs. By defining an indexing system for the hexagonal lattice structure we were able to define the Kirigami designs as 2D matrix for numerical implementation. We digitalized two different macroscale designs, which we named the *Tetrahedron* and *Honeycomb* pattern respectively, that successfully produced out-of-plane buckling when stretched. Through a numerical framework we could create an ensemble of perturbed variations which gave approximately 135k configurations for the Tetrahedron pattern and 2025k patterns for the size of the sheet used in our study. When considering the possibility to translate the patterns this gave roughly a factor 100 more of unique pertubations. We also created a framework for creating Kirigami designs through a random walk. This was further controlled by introducing features such as bias, avoidance of existing cuts, preference to keeping a direction and procedures to repair the sheet for simulation purposes. The capabilities of the numerical framework for generating Kirigami designs was far larger than the capabilities for producing MD designs within the time constraint of this thesis. Thus we believe that this contains the possibility to benefit more extended studies and for the creation of a larger dataset.

2.1.3 Control friction using Kirigami

We find buckling in vacuum which correspond ot a reduciton in contact area in connection with a substrate. We find the honeycomb to buckle most resulting in a reduction of the contact area to approximately 43%.

We have investigated the friction behavior of the non-cut sheet and a selected Tetrahedron and Honeycomb pattern under various stretch and load. The non-cut sheet did not exhibit significant out-of-plane buckling as opposed to the Tetrahedron and Honeycomb pattern. This is even when considering that the non-cut sheet had a yield strain of 0.35 while the Tetrahedron had a lower yield strain of 0.21 and the Honeycomb a considerable larger one at 1.27 based on a stretch in vacuum. The out-of-plane buckling resulted in a signifciant reduction of the contact area as the sheet were stretched, towards a minimum of X for the Tetrahedron and y for the Honeycomb pattern. However, this disagreed with the asperity theory hypothesis of a decreasing friciton with decreasing contact area. We found that the strain-induced buckling was initially (at low relative strain) assocated with an increase in friction. Moreover, the friction-strain curve produced a no-linear behaviour which was not compatible with the approximately monotonic decreasing contact area as strain were increased. This is shown in Fig. 1.13. This led us to the conclusion that the contact area cannot be attributed a dominant mechanism for friction throughout the straining of the studied Kirigami sheets. In general we found a non-existing relationship between friction and load considering the uncertainties in the simulation. This is best attributed to the superlubric state of the graphene sheet on the substrate. The slope of the friction-load curves were not significantly affected by the straining of the Kirigami sheet and thus we conclude that the load effect on friction is neglible cimpared to the strain effects.

2.1.4 Capture trends with ML

With the use of MD simulations, we have generated an extended dataset of 9660 data points based on 216 Kirigami configurations (Tetrahedron: 68, Honeycomb: 45, Random walk: 100, Pilot study: 3) under various strains and normal loads. The dataset reveals some general correlations with mean friction, such as a positive correlation to strain (0.77) and porosity (0.60), and a negative correlation to contact area (-0.67). These results align with the findings from the pilot study suggesting that these features are relevant, but not necessarily the cause, of the observed phenomena. By defining the friction property metrics: $\min F_{\text{fric}}$, $\max F_{\text{fric}}$, $\max \Delta F_{\text{fric}}$ and max drop (maximum decrease in friciton with strain), we investigated the top candidates within our dataset. From these results, we found no incentive of the possibility to reduce friction with the Kirigami approach since the non-cut sheet provided the lowest overall friction. Regarding the maximum properties, we found an improvement from the original pilot study values and with the Honeycomb pattern producing the highest scores. This suggests that the data contains some relevant information for optimization with respect to these properties. Among the top candidates, we found that a flat friction-strain profile is mainly associated with little decrease in the contact area and vice versa.

For the machine learning investigation, we have implemented a VGGNet-16-inspired convolutional neural network with a deep "stairlike" architecture: C32-C64-C128-C256-C512-C1024-D1024-D512-D256-D128-D64-D32, for convolutional layers C with the number denoting channels and fully connected (dense) layers D with the number denoting nodes. The final model contains 1.3×10^7 and was trained using the ADAM optimizer for a cyclic learning rate and momentum scheme for 1000 epochs while saving the best model during training based on the validation score. The model validation performance gives a mean friction R^2 score of $\sim 98\%$ and a rupture accuracy of $\sim 96\%$. However, we got lower scores for a selected subset of the Tetrahedon ($R^2 \sim 88.7\%$) and Honeycomb ($R^2 \sim 96.6$) pattern based on the top 10 max drop scores respectively. These scores were lower despite the fact that the selected set was partly included in the training data as well and the fact that the hyperparameter selection favored the performance on this selected set. Thus we conclude that these selected configurations, associated with a highly non-linear friction-strain curve, represent a bigger challennge for machine learning prediction. One interpretation is that these involve the most complex dynamics and perhaps that this is not readily distinguished from the behavior of the other configurations which constitutes the majoriry of the data set. By evaluating the ability for the model to rank the dataset according to the property scores we found in general a good representation of the top 3 scores for the maximum categories, while the minimum friction property ranking was lacking. We attribute this latter observation to a higher need for precision in order to rank the lowest friction values properly which the model did not possess.

In order provide a more true evaluation of the model performance we created a test set based on MD simulations for an extended Random walk search. This test revealed a significantly worse performance than seen for the validation set with a two-order of magnitude higher loss and a negative friction mean R^2 score which corresponds to the prediction being worse than simply guessing on a constant value based on the true data mean. However, by considering one of the early hypertuning choices, regarding architecture complexity, we evaluated the model when prioritizing mainly for the lowest validation loss. This gave similar performance on the test set which indicates that it is not simply a product of a biased hypertuning process, since we based our choices on the selected confgiruation set (which overlapped with the training data). Instead, it points to the fact that our original dataset did not cover a wide enough configuration distribution to accurately capture the full physical complexity of the Kirigami friction behavior.

2.1.5 Accelerated search

Using the ML model we performed two types of accelerated search. One by evaluating the property scores of an extended dataset and another with the use of the genetic algorithm approach. For the extended dataset search we used the developed pattern generators to generate 135 k × 10 Tetrahedon, 2025 k × 10 Honeycomb and 10 k Random walk patterns. For the minimum friction property, the search suggests a favoring of a low cut density (low porosity) which aligns with the overall idea that the dataset does not provide an incentive for further friction reduction. The maximum properties resulted in some minor score increases but the suggested candidates were overlapping with the original dataset. By investigating the sensitivity to translation of the Tetrahedron and Honeycomb patterns we found that the model predictions varied drastically with pattern translation. This can be attributed to a physical dependency since the edge of the sheet is effected by this translation. However, due to the poor model performance on the test set, we find it more likely to be a model insufficienty arising from a lacking training dataset.

For the genetic algorithm approach, we investigated the optimization for the max drop property with respect to starting population based on the result from the extended dataset accelerated search, and some random noise initializations with different porosity values. This approach did not provide any noteworthy incentive for new design structures worth more investigation. In general, the initialization of the population itself proved to be a more promising strategy tha the genetic algroithm. However, this is highly affected by the uncertainty of the model predictions, and thus we did not pursue this any further. By considering the Grad-CAM explanation method we found that the model predictions sometimes seem to pay considerable attention to the top and bottom edge of the configurations. This is surprising since these are not true edges but are connected to the pull blocks in the simulation. Despite the uncertainties in the predictions, we argue that this might be attributed to thermostat effects from the pull blocks and thus we note this as a feature worth more studying.

2.1.6 Negative friction coefficient

By enforcing a coupling between load and stretch, mimicking a nanomachine attached to the sheet, we investigated the load curves arising from loading of the Tetrahedron $(7, 5, 1)$ and Honeycomb $(2, 2, 1, 5)$ pattern from the pilot study. The non-linear trend observed for increasing strain carried over to the coupled system as well producing a highly non-linear friction-load curve. This demonstrates a negative friction coefficient say something about the values.

2.2 Outlook / Perspective

Having successfully demonstrated a non-linear effect on friction with increasing strain of the sheet our results invite a series of further studies to investigate this relation. First of all, it would be valuable to investigate how the friction-strain curve depend on temperature, sliding speed, spring constant, and on load for an increased range $F_N > 100nN$. This is especially interesting in the context up conditions leading to a stick-slip behvaior as our results were carried in the smooth sliding. Moreover, it would be important to verify that the choices for relaxation time and pauses are not critical for the qualitative observations as well as trying a different interatomic potential for the graphene and perhaps an entirely different substrate material. Especially the Adaptive Intermolecular Reactive Empirical Bond Order (AIREBO) potential for the modeling of the graphene sheet might be of interest. The effects from excluding adhesion (the LJ interaction) can also be useful for the investigation of the observed phenomena.

In order to get a better understanding of the underlying mechanism for the friction-strain relationship we might investigate commensurability effects further by varying the scan angle. we might also consider investigating the friction-strain relationship under a uniform load to get insight into whether the loading distribution is of importance. Another topic worth studying is the relation to scale. Thus it would be interesting to study size effects but also further look into edge effects by translating the pattern. With this regard, we would also suggest a more detailed study of the effect from the thermostat in the pull blocks which is suggested to have a possibly importance by judging from the machine learning model Grad-CAM analysis.

For machine learning, we can either try to extend the data set to resolve the issue of the model not being generalized enough. We can also create a dataset for a single kirigami design and include some of the mentioned physical variables above and attempt to use machine learning for unraveling these relations. In that context we would advice for as more detailed investigation of machine learning techniques. If succesfull this would invite a study of inverse design methods such as GAN or diffusion models.

- How is this behavior effected by scaling?
- How does the distirbution of normal load effect the Kirigami friction behavior?
- Things to vary: load range, scan directions, adhesive forces, longer relaxation time, different potential (AIREBO)
- Investigate if the contact area is effecting the friciton non-linear by turning of friction force for atoms corresopnding to those that lift of from the sheet during the out-of-plane buckling.
- Investigations of commensurability effects.
- Study dependency of translation of the patterns as suggested by the ML results.
- Investigate effects from pull blocks...
- Investigate effects from the thermostat since the top and bottom edges was shown interest by the model prediction.

Appendices

Appendix A

Appendix A

Appendix A

Appendix B

Appendix B

Appendix C

Bibliography

[1] S. Li, Q. Li, R. W. Carpick, P. Gumbsch, X. Z. Liu, X. Ding, J. Sun, and J. Li, “The evolving quality of frictional contact with graphene”, Nature **539**, Number: 7630, 541–545 (2016).

[2] H. M. Yoon, Y. Jung, S. C. Jun, S. Kondaraju, and J. S. Lee, “Molecular dynamics simulations of nanoscale and sub-nanoscale friction behavior between graphene and a silicon tip: analysis of tip apex motion.”, Nanoscale **7 14**, 6295–303 (2015).

[3] Y. Liu, F. Grey, and Q. Zheng, “The high-speed sliding friction of graphene and novel routes to persistent superlubricity”, Scientific Reports **4**, 4875 (2014).

[4] P. Zhu and R. Li, “Study of nanoscale friction behaviors of graphene on gold substrates using molecular dynamics”, Nanoscale Research Letters **13**, 34 (2018).

[5] J. Zhang, E. Osloub, F. Siddiqui, W. Zhang, T. Ragab, and C. Basaran, “Anisotropy of graphene nanoflake diamond interface frictional properties”, Materials **12**, `10.3390/ma12091425` (2019).

[6] F. Bonelli, N. Manini, E. Cadelano, and L. Colombo, “Atomistic simulations of the sliding friction of graphene flakes”, The European Physical Journal B **70**, 449–459 (2009).

[7] S. Zhang, Y. Hou, S. Li, L. Liu, Z. Zhang, X.-Q. Feng, and Q. Li, “Tuning friction to a superlubric state via in-plane straining”, Proceedings of the National Academy of Sciences **116**, Publisher: Proceedings of the National Academy of Sciences, 24452–24456 (2019).

[8] J. H. Dieterich, “Time-dependent friction in rocks”, Journal of Geophysical Research (1896-1977) **77**, 3690–3697 (1972).

[9] H. Tomaç, Z. Guchan, and N. Altun, “How the stiletto heeled shoes which are popularly preferred by many women affect balance and functional skills?”, Health Care for Women International **43**, 1–11 (2020).

[10] K. Gibbs, *Pressure*, (2020) `https://www.schoolphysics.co.uk/age16-19/Mechanics/Statics/text/Pressure_/index.html`.

[11] F. B. Ltd, *Foot facts*, (2023) `https://www.footbionics.com/Patients/Foot+Facts.html`.

[12] M. Dienwiebel, N. Pradeep, G. S. Verhoeven, H. W. Zandbergen, and J. W. Frenken, “Model experiments of superlubricity of graphite”, Surface Science **576**, 197–211 (2005).